Effect of chlorine and bromine on the perovskite crystal growth in mesoscopic heterojunction photovoltaic device

Hanadi Mehdi [1,2*], Lucia Nicoleta Leonat [2, *],Hamza Saidi[1], Viorica Stancu [2], Monica Enculescu[2], Andrei-Gabriel Tomulescu[2], Vasilica Toma[2] Abdelaziz Bouazizi[1] , Ioana Pintilie[2] and Aurelian Catalin Galca [2]

[1] Group of Organic Electronic and Molecular Photovoltaics Devices, Laboratory of Condensed Matter and Nanosciences, Faculty of Sciences of Monastir, University of Monastir, ,5019 Monastir, Tunisia

[2] Laboratory of Multifunctional Materials and Structures, National Institute of Materials Physics, Atomistilor 405A, 077125 Magurele, Ilfov, Romania

Corresponding authors: *hanadi.mehdi92@gmail.com ; lucia.leonat@infim.ro*

Keywords: chlorine, bromine, crystal growth, organic-inorganic perovskite solar cells

Abstract

Organic-inorganic hybrid perovskite solar cells are within the emerging photovoltaic technologies. The combination of different halogen ions, in certain fill fractions, is one of the methods to improve the perovskite film properties. Herein, fabrication and characterization of perovskite cells in standard mesoscopic architecture using one-step deposition method has been done. The role of the halogen ions (Chlorine or Bromine) on crystal structure growth and photoelectric performance has been investigated. X-ray diffraction, scanning electron microscopy, atomic force microscopy and optical microscopy analysis were performed.

1. Introduction

Organic-inorganic hybrid perovskite solar cells (PSCs) have attracted significant attention as a promising material for photovoltaic applications due to their photo-physical properties, high defect tolerance, a tunable band gap by compositional engineering, and their simple solution fabrication process using low-cost materials [1-7]. Their high-power conversion efficiency (PCE) has achieved an impressive improvement, and presently the best cells go beyond 25% [8,9].

Methylammonium lead triiodide ($CH_3NH_3PbI_3$) is one of the most studied perovskite materials in photovoltaics perovskite field. The perovskite solar cells based on this perovskite type has demonstrated the relevant stable and efficient devices [10-12]. The heterojunction solar cells based on $CH_3NH_3PbI_3$ have a considerable advantage in terms of synthesis and performance, in combination with mesoporous TiO_2 as electron transport layer and spiro-OMeTAD and hole transport layer [13,14].

Improving the morphology, homogeneity and microstructure of the perovskite film are among the most important assements to obtain devices with high efficiency. Many scientific publications state that the photovoltaic performance of PSCs is directly correlated with the perovskite deposition parameters, such as the annealing treatment [15-17], the molar ratio of the precursors [18-20] and the deposition procedure [21-23]. Other studies suggest that for an easy to scale-up "one-step" deposition process, the $CH_3NH_3PbI_3$ hybrid perovskite must contain small amounts of chloride or bromide [24-28].

Recently, it has been suggested that compositional engineering by using other halogens such as chlorine (Cl) or bromine (Br), which leads to mixed halide perovskites, is one of the most used strategies to improve the PCE in solar cells [29-44]. On the other hand, the band gap of the perovskite depends on halogens concentrations [45-47], while the choice of organic cations impacts the stability of the devices [48-50].

The addition of Br and/or Cl increases the generation and diffusion length of the carriers, reducing charge recombination in the perovskite absorber film, leading to better photovoltaic performance [24]. Moreover, Cl and Br slow down the nucleation process and speed up the crystal growth rate, thus, having a impact on the microstructure (crystallinity) of the perovskite film [51, 52]. Br ions have a higher activation energy of the ionic migration than I ions, and consequently, reduced movement within the perovskite film, while Cl ions improve the diffusion length of the free carriers [53]. Therefore, mixing the halogens in the perovskite structure is a key to obtain superior photovoltaic properties with lower hysteresis effects than devices with $CH_3NH_3PbI_3$ only [54,55]. Previous work has demonstrated the potential of the mixt halide perovskite with different ratios to provide more stable and more efficient devices. For example, for perovskites I and Cl halogen mixtures, *Tombe et al.* [56], *Po-Wei Liang et al* [57] and *Spalla et al* [58] reported their work with planar inverted geometry devices.

This paper focuses on the mixt halogenated perovskites with either I : Cl or I : Br in the same proportion of 1.8:1.2. This work focuses on the perovskite films with the composition $CH_3NH_3PbI_{1.8}Br_{1.2}$, and how the properties of the perovskite film change when Cl is used instead of Br in the same amount. The role of the halogen's composition on the morphology, microstructure, and optical properties as well as on photovoltaic performance and stability in solar cells in a mesoscopic geometry is studied.

2. Experimental section

2.1. Materials

Pre-cut fluorine tin oxide (FTO, 2.5x 1.5 cm^2) coated glass with a sheet resistance of 15Ω/sq were purchased from Xin Yan Technology LTD, China. Lead chloride ($PbCl_2$, 99.99%), lead Bromide ($PbBr_2$, 99.99%), N,N-Dimethylformamide (DMF), Dimethylsulfoxide (DMSO), Chlorobenzen (CB), acetone, isopropanol (IPA) and anhydrous ethanol, 4-tert-butylpyridine (tBP, 99.99%) and titanium diisopropoxide bis(acetylacetonate) ($Ti(iProp)_2AcAc_2$ were purchased from Sigma Aldrich. Methylammonuim iodide (MAI, 99%) was purchased from Dyesol. Ti-Nanoxide T/SP was purchased from Solaronix, Spiro-OMeTAD (99.99%) was purchased from Borun Chemicals, China.

2.2. Preparation of the precursor perovskite solutions

The $MAPbI_{1.8}Cl_{1.2}$ solution was prepared by dissolving, MAI (159 mg), PbI_2 (184.40 mg), $PbCl_2$ (166.86 mg) in DMF: DMSO (8:1) mixture. The second perovskite solution $MAPbI_{1.8}Br_{1.2}$ was prepared by dissolving, MAI (159 mg), PbI_2 (184.40 mg), $PbBr_2$ (220.21 mg) in DMF: DMSO (8:1) mixture. The solutions were left to stir for 24 hours at room temperature before deposition under nitrogen atmosphere.

2.3. Solar cell fabrication

The mesoscopic PSCs: FTO/$TiO_{2c\text{-}m}$/perovskite/Spiro-oMeTAD/Au was elaborated according to the following procedure:

First the FTO-coated glass slides were cleaned with a detergent solution and rinsed with plenty of distilled water, followed by sonication in acetone and then in isopropanol in an ultrasonic bath for 10 min for each solvent. Before the (c-TiO_2) compact layer deposition, the FTO/Glass substrates were exposed to O_2 plasma treatment for 10 min.

The compact TiO_2 (c-TiO_2) was then deposited by spray pyrolysis, using $Ti(iProp)_2AcAc_2$ in IPA (1:30 molar ratio), holding in the meantime the substrates on a hot plate at 450°C, followed by annealing treatment at 450°C for 30 min. Mesoporous TiO_2 films were deposited by spray coating a precursor colloidal solution consisting of commercial 20 nm-sized particles dispersed in anhydrous ethanol at 1:200 weight ratio, while the substrates were kept on a hot plate at 100°C during pulverization. After deposition, all final substrates were placed in a furnace for 1 h at 500°C.

The perovskite solutions with the different concentrations were spin coated at 2000 rpm for 25s. While spinning, after the first 15 s, ~150 μL of CB was dropped to facilitate perovskite crystallization. Then, the perovskite films were annealed at 100 °C for 3 min.

A mixture of 80 mg spiro-OMeTAD, 28 μL 4-tert-butylpyridine, and 18 μL of bis(trifluoromethane) sulfonimide lithium salt in acetonitrile solution (520 $mg.ml^{-1}$), were dissolved in 1 mL chlorobenzene. This solution was spun at 3000 rpm for 30s over the perovskite surface.

Finally, the gold electrodes (80 nm thickness, 0.083 cm^2 surface area) were deposited on top of structures by *rf* magnetron sputtering in argon atmosphere at 3.10^{-3}mbar, through a shadow mask.

The schematic illustration of the mesoscopic standards perovskite solar cell is shown in Figure.1.

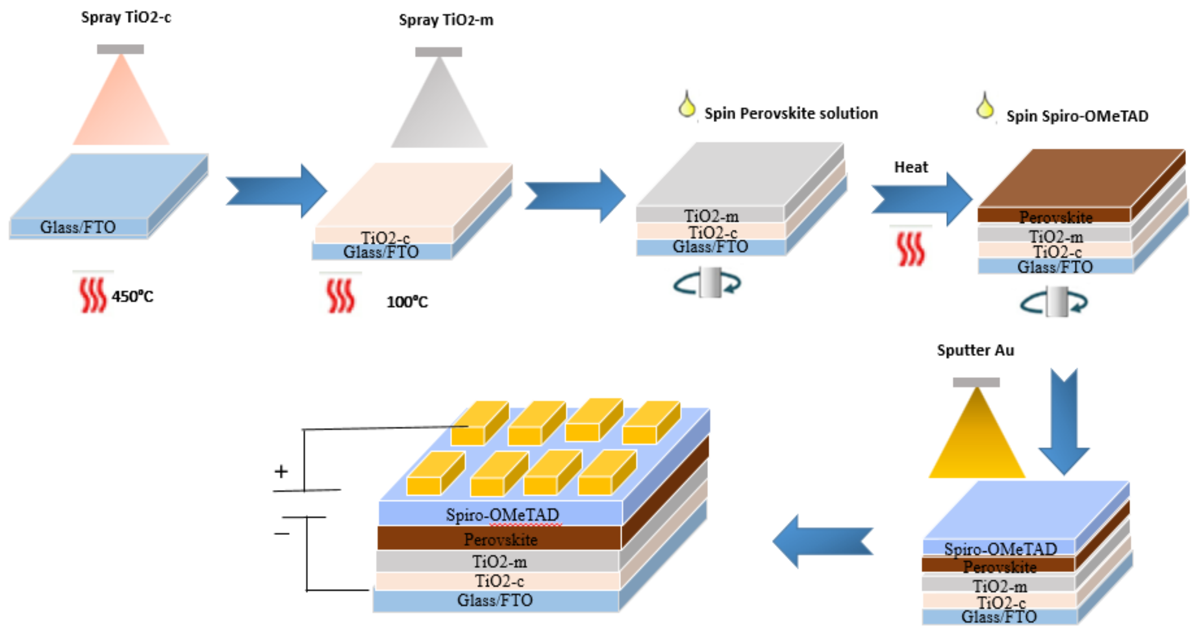

Figure 1. Schematic of device fabrication process and the structure of a complete "standard" mesoscopic solar cell.

2.4. Characterization

The X-ray diffraction (XRD) patterns of the thin films were measured by a Bruker-AXS Advance diffractometer using Cu anode (λ=1.54 Å). The UV–vis spectra were collected using a conventional spectroscopy mode using a V-Vase Woollam spectroscopic ellipsometer equipped with a high-pressure Xe discharge lamp incorporated in an HS-190 monochromator. Photoluminescence spectra have been recorded at room temperature using a FluoroMax 4Pspectrophotometer with excitation light having an oblique angle of incidence (selected wavelength λ_{exc}=450 nm). Scanning Electron Microscopy images were inspected by Zeiss GeminiSEM-500. Optical microscopy images were obtained with a Zeiss microscope. Surface morphologies were also investigated by atomic force microscopy (AFM) (NTMDT Aura Ntegra Prima Station, samples were scanned in non-contact mode). The current–voltage characteristics for the solar cells were measured under AM 1.5G, 100 mW cm2 simulated sunlight OrielLSH-7320, Class ABA LED Solar Simulator coupled with a Keithley 2601B Source Meter) in forward and reverse scan direction.

The current–voltage characteristics for the solar cells were measured under AM 1.5G, 100 mW/cm^2 simulated sunlight OrielLSH-7320, Class ABA LED Solar Simulator coupled with a Keithley 2601B Source Meter) in forward and reverse scan direction. The solar simulator was calibrated with an NREL-certified KG5-filtered Si reference diode to an irradiation intensity of 100mW/cm^2. Electrical measurements were performed outside in ambient environment, at room temperature (<25^{o}C), starting first in reverse direction, just above the Voc to Jsc, to avoid unintentional prepoling according to the procedure described elsewhere [59] of the samples and backward (towards positive voltage direction), at 20 mV/s. All devices were measured in ambient environment without encapsulation.

3. Results

3.1. X-ray diffraction

X-ray diffraction studies were conducted to investigate the microstructure of the perovskite layers and the resulted graphs are presented in figure 2. Multiple diffraction peaks indicate that the films are polycrystalline.

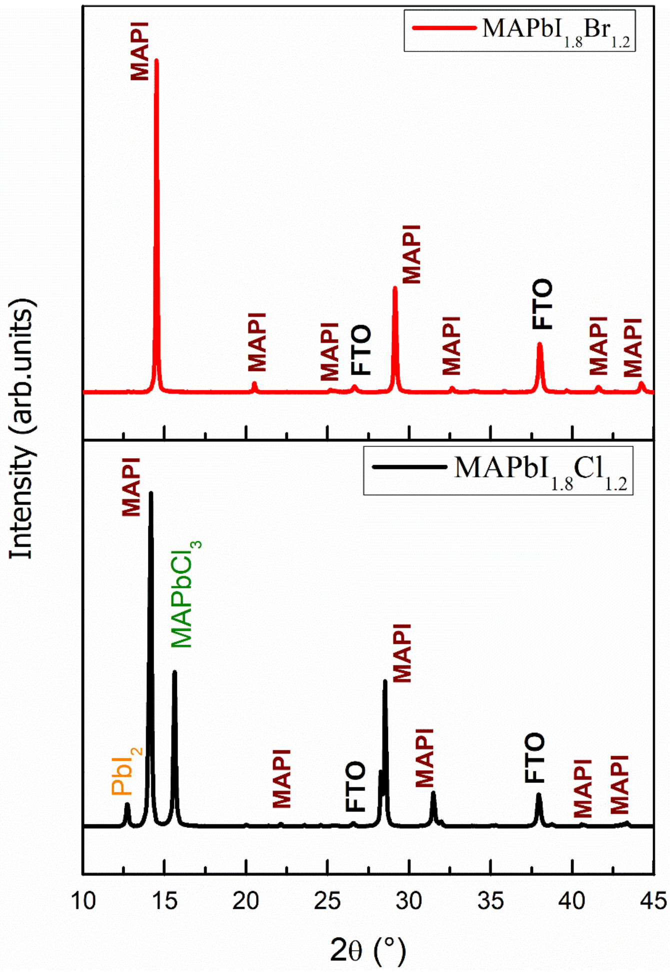

Figure 2. XRD patterns of the elaborated perovskite layers with different halogens composition a) $MAPbI_{1.8}Br_{1.2}$ and b) $MAPbI_{1.8}Cl_{1.2}$

The typical diffractogram of the perovskite films with chlorine, $MAPbI_{1.8}Cl_{1.2}$, presents a well-crystallized primary phase with tetragonal structure, with the characteristic peaks of parent $MAPI_3$ at 14.15° (002/110), 20.08° (200), 23.55° (211), 24.55° (202), 28.52° (004/220), 31.90° (310), 35.07° (312), 40.79° (400) and 43.31° (330) according to ICDD 01-084-7607. In addition, the presence of two other minor secondary phases of unreacted lead iodide (PbI_2) at 12.7° (ICDD 00-007-0235) and segregated $MAPbCl_3$ perovskite at 15.7° (ICDD 01-085-5450) [60, 61], are observed.

The samples with bromine ($MAPbI_{1.8}Br_{1.2}$) have a cubic structure, similar to $MAPbBr_3$ - ICDD 00-069-1350 [62], inferred also from the symmetry of the 001 and 002 reflections. Since the largest instrumental errors are present at smaller 2θ angles, we focused our analysis of the average crystallite size and lattice parameters on the peaks observed in the 28-30 angles range. The results are presented in table 1. Figure 3 presents the zoomed XRD patterns of the main peaks along with the fitted Lorentzian components.

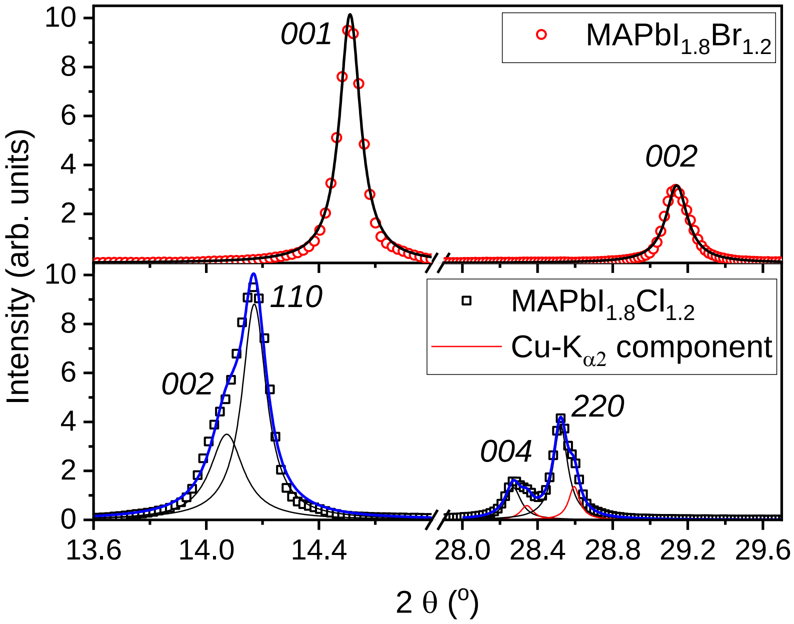

Figure 3. Zoomed XRD patterns and component peaks /fits of each resulted from Lorentz function fitting routine of 001 and 002 for the MAPbI$_{1.8}$Br$_{1.2}$ and 002/110 and 004/220 for the MAPbI$_{1.8}$Cl$_{1.2}$

As stated above, MAPbI$_{1.8}$Br$_{1.2}$ characteristic peaks do not indicate any asymmetry. Contrary, MAPbI$_{1.8}$Cl$_{1.2}$ peaks are asymmetric, the splitting being clear for 004/220 reflections, thus confirming the cubic structure for the Br samples, and the tetragonal structure for the Cl ones. The main difference between the two XRD spectra in Figure.3 is the considerable shift of the diffraction lines as well as the difference in the crystal structure [63].

Table 1. Lattice parameters of the diffraction planes for the two different compositions.

Composition	Reflection hkl	2 Θ(°)	w_{exp}(°)	w_{ins} (°)	D(nm)
MAPbI$_{1.8}$Br$_{1.2}$	002	29.14	0.141	0.063	117
MAPbI$_{1.8}$Cl$_{1.2}$	004	28.27	0.101	0.063	237
	220	28.52	0.093	0.063	296

The crystallite size of this different composition was determined by the Debye-Scherrer formula, and listed in Table 1:

$$D = \frac{K\lambda}{\mathbf{w\cos\Theta}} \qquad \textbf{eq. 1}$$

where D is the crystallite size, λ is the X-ray wavelength in nanometers (nm), *w* is the peak width of the diffraction peak profile at half maximum height (calculated after subtracting the full width at half maximum characteristic for the instrument w_{ins} from the experimental w_{exp}), K is a constant related to the crystallite shape taken as 0.94 and D_{ave} is the average crystallite size of the film [64]. The calculated average crystallite size of $MAPbI_{1.8}Br_{1.2}$ and $MAPbI_{1.8}Cl_{1.2}$ were 117 nm and 267 nm respectively.

The full width at half maximum (w) of the *002*-characteristic peak in the XRD patterns from the $MAPbI_{1.8}Br_{1.2}$ film appears sharper (w: 0.141°) than that from the *004/220* characteristic peak of $MAPbI_{1.8}Cl_{1.2}$. (w: 0.101 and 0.093°), as shown in Table 1. A lower FWHM value is noted for the formulation with Cl^-, which indicates larger crystallites [65].

However, the perovskite films with chlorine presents a detectable amount of PbI_2 secondary phase, by the presence of the diffraction line at 12.27°. No residual PbI_2 diffraction peaks were noted in the brominated-iodine perovskite film as shown in Figure 2, suggesting the complete conversion of the precursors to perovskite. Most likely, the incorporation of bromine has increased the speed of the crystallization process of perovskite thus stopping the formation of the PbI_2 salt.

This difference is not attributed to the higher ionic radius of Br (0.196 nm) relative to Cl (0.185 nm), which results in a very slight decrease of the Goldschmidt tolerance factor *t*, of the perovskite structure from 0.918 for the $MAPbI_{1.8}Cl_{1.2}$ and to 0.915 for $MAPbI_{1.8}Br_{1.2}$, respectively, calculated by:

$$t = \frac{(rA + rX)}{\sqrt{2}\,(rB + rX)} \qquad \textbf{eq.2,}$$

where r_A r_B and r_X are the ionic radii for A, B and X. The other ionic radii taken for calculation are of MA^+ (0.216 nm), Pb^{2+} (0.119 nm), and I^- (0.220 nm [66,67].

3.2. Optical microscopy

Surface topography and roughness of the prepared perovskite films were inspected by optical microscopy, AFM and SEM in Figure.4, Figure 5 and Figure 6.

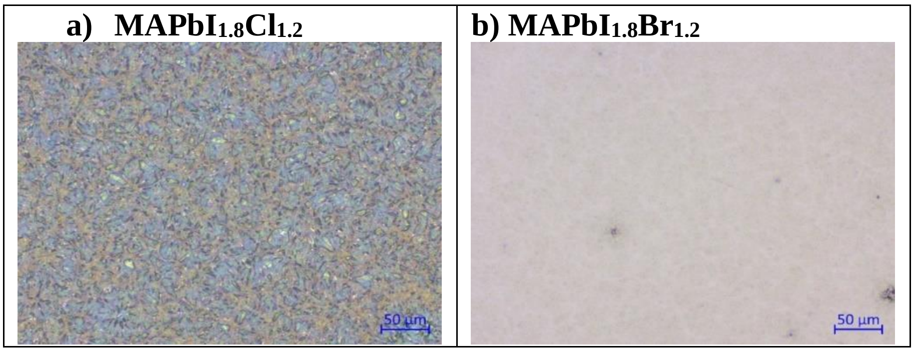

Figure 4: Optical microscopy images of the perovskite films prepared with chlorine (a) and bromine (b).

Figure 4 shows the optical microscopy images of the perovskite films prepared of the two type of perovskite films. The surface coverage as well as the grain morphology are different for the two solutions. The effect of the chlorine and bromine halides can be observed. The

$MAPbI_{1.8}Cl_{1.2}$ films (Figure (4ba)), show a structure with uneven, inhomogeneous surface. The crystals are agglomerated in different areas, and therefore, the perovskite film does not cover the entire substrate surface, since the TiO_2 under layer is visible. However, for the sample with bromine Figure (4b), the perovskite film looks homogeneous, providing uniform coverage of the TiO_2.

3.3. Atomic force microscopy

Atomic force microscopy was used to explore the surface morphology of the prepared films. Figure 4 shows the AFM images for the mixed halide perovskite films fabricated onto TiO_{2m} with chlorine and bromine.

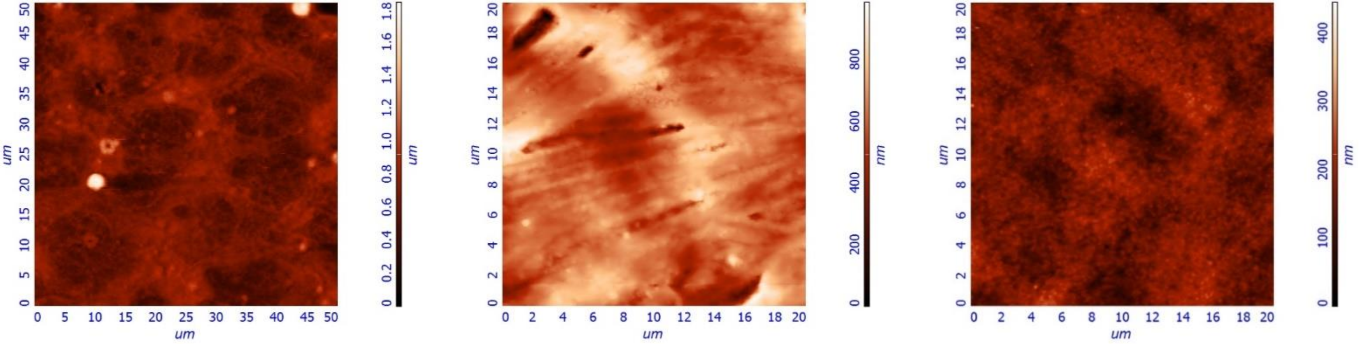

a) TiO_2 mesoporous **b) $MAPbI_{1.8}Cl_{1.2}$** **c) $MAPbI_{1.8}Br_{1.2}$**

Figure 5. AFM images of: a) mesoporous TiO_2 layer and perovskite layers: b) $MAPbI_{1.8}Cl_{1.2}$ and c) $MAPbI_{1.8}Br_{1.2}$

$MAPbI_{1.8}Cl_{1.2}$ films have a relatively ordered surface with needles-shaped features shown in Figure 5a). The root mean square (RMS) calculated for a 20x20 µm area is 112 nm. The image shows a dendritic structure with tightly packed needle-like shapes and the voids between them, evidence of an incomplete surface coverage, with a negative impact on the performance of the device.

Table 2. Surface parameters extracted from AFM images analysis for the different samples

Solution	Root mean square, RMS (nm)	Average roughness Sa (nm)
TiO_2 mesoporous	136	98
$MAPbI_{1.8}Cl_{1.2}$	112	86
$MAPbI_{1.8}Br_{1.2}$	31	25

In comparison, the typical AFM topographical image of the $MAPbI_{1.8}Br_{1.2}$ film (Figure 5c) shows a dense and smooth film, with an RMS roughness of only 31 nm, an order of magnitude smoother than the Cl perovskite film. At the same time, the TiO_2 rough shape is smoothened by the thick, compact brominated perovskite. This improvement of the surface coverage supports the carrier mobility and transport, within the perovskite film but also at the interface with the mesoporous, which further leads to higher device efficiency [68, 69].

3.4. Scanning Electron Microscopy

The two different surface morphologies of the perovskite films were investigated by scanning electron microscopy (SEM) and shown in Figure 6.

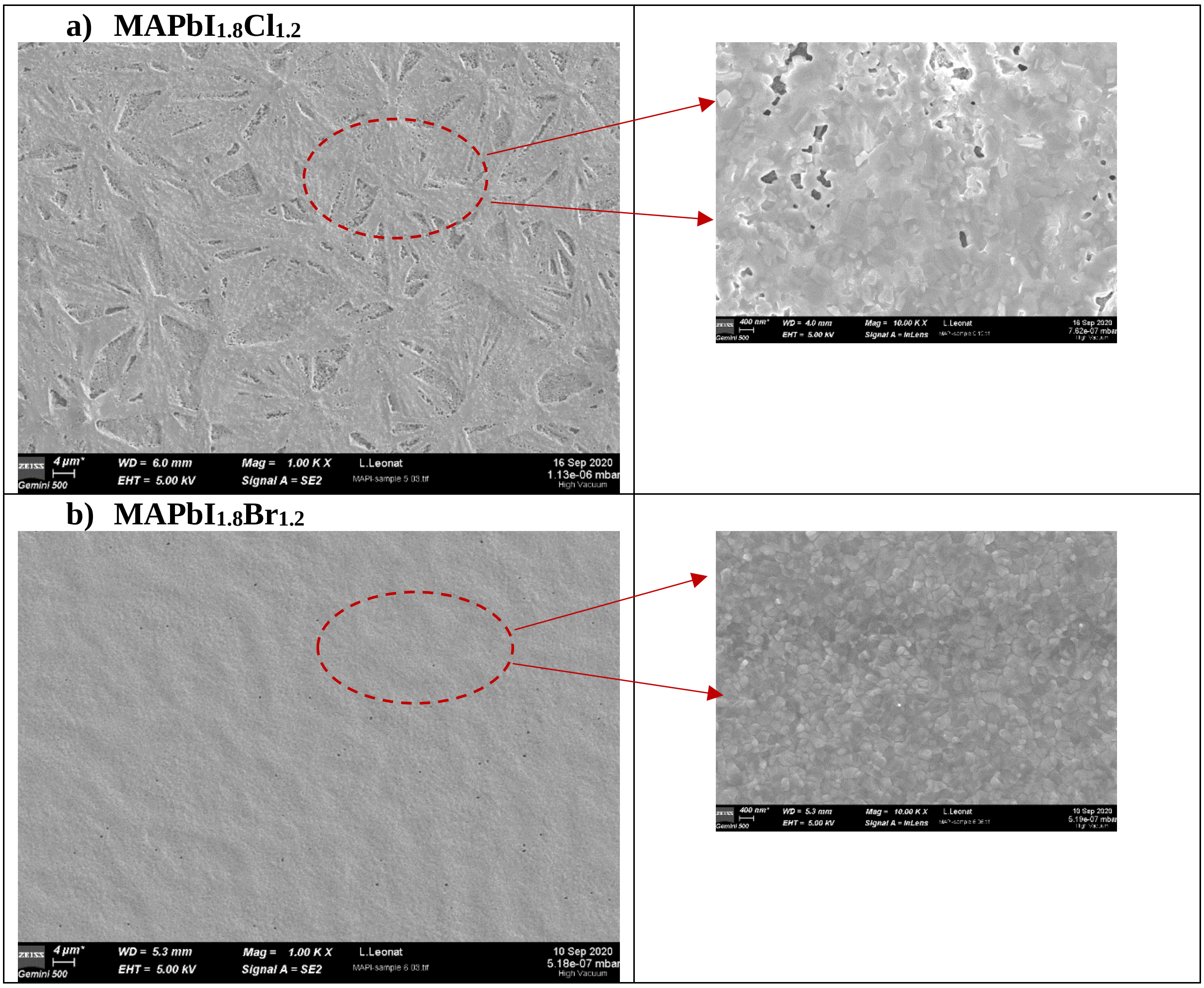

a) MAPbI$_{1.8}$Cl$_{1.2}$

b) MAPbI$_{1.8}$Br$_{1.2}$

Figure 6. Surface morphologies of perovskite films: a) MAPbI$_{1.8}$Cl$_{1.2}$ and b) MAPbI$_{1.8}$Br$_{1.2}$.

The MAPbI$_{1.8}$Cl$_{1.2}$ film shows a partially compact surface with large void-defects, as shown by the SEM images in Figure 6a. Moreover, the dendritic growth of the crystalline films based on iodine and chlorine mixture, shows an aggressive crystallization, with distinct areas containing tightly packed crystallites in the form of branches and in between them, micron-sized large gaps, thus resulting a discontinuous perovskite coverage. It is widely accepted that the formation of such films is sensitive to the thermal annealing conditions, such as time and temperature) [70,71]. This specific morphology can originate from the differences in grain nucleation and crystal growth between the Cl and Br containing films. This is in good agreement with the XRD measurements in which the $MAPbI_{1.8}Cl_{1.2}$ shows a larger crystallite size compared to that of the $MAPbI_{1.8}Br_{1.2}$ [72]. Notably the needle-like crystalline PbI_2 vaguely appeared on the perovskite surfaces, which is likewise confirmed by the recorded XRD pattern shown in Figure.2.

In the case of the $MAPbI_{1.8}Br_{1.2}$ perovskite (Figure 6b), the film morphology looks completely different regarding grain order and film coverage. The SEM image reveals a uniform film with dense nano-sized crystal domains. Additionally, reducing pinholes eliminates the possibility of direct contact between adjacent p- and n-type charge selective layers preventing device short-circuit.

3.5. Optical properties

To investigate the influence of halogens, the derivatives UV-visible absorption and photoluminescence spectra were reported for the perovskite films made from different solutions and elaborated on FTO/TiO_2-cm substrates. (Figure 7).

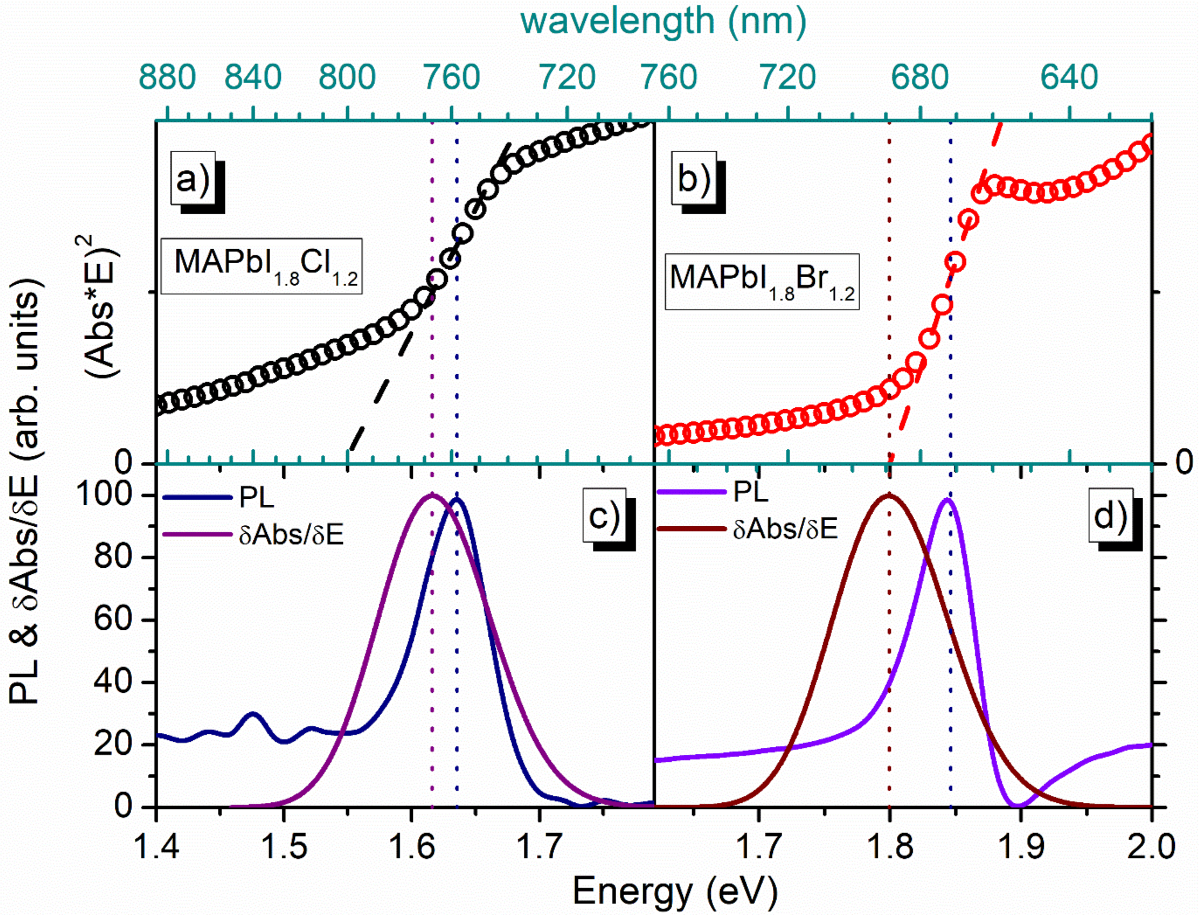

Figure 7: a,b) Optical band gap determined from linear fits of the Tauc plot; c,d) normalized Photoluminescence and Vis-NIR absorbance derivatives spectra of the $MAPbI_{1.8}Cl_{1.2}$ and $MAPbI_{1.8}Br_{1.2}$ respectively.

From the curves in Figure 7, the band gap was calculated for each of the two compositions. It is observed that when a halogen with higher electronegativity is chosen, the affinity with the

Pb ion increases, thus reducing the ionic character of the halogen-Pb bond in favor of the covalent character of the bond, leading to a redshift of the optical absorption curves.

The absorption spectra for halide perovskite has shifted to lower wavelength by changing the halide from Cl to Br. The E_g shift of of $MAPbI_{1.8}Cl_{1.2}$ compared with $MAPbI_{1.8}Br_{1.2}$ is due to the decrease in the covalent character of the halogen bonding with Pb, which means a decrease in the electron negativity of the halogen [73,74].

Analogously, the normalized PL emission peak show same behavior while Br doping leads to a detectable red shift, and the Pl emission peak shifted from 690 nm to 768 nm.

Meanwhile, this shift behavior of the photoluminescence peak can be explained by the formation of ordered crystals. The red-shift of the PL emission of the hybrid perovskite material has been reported to occur due to the crystallization of the perovskite [75] and observed by other groups as well [76].

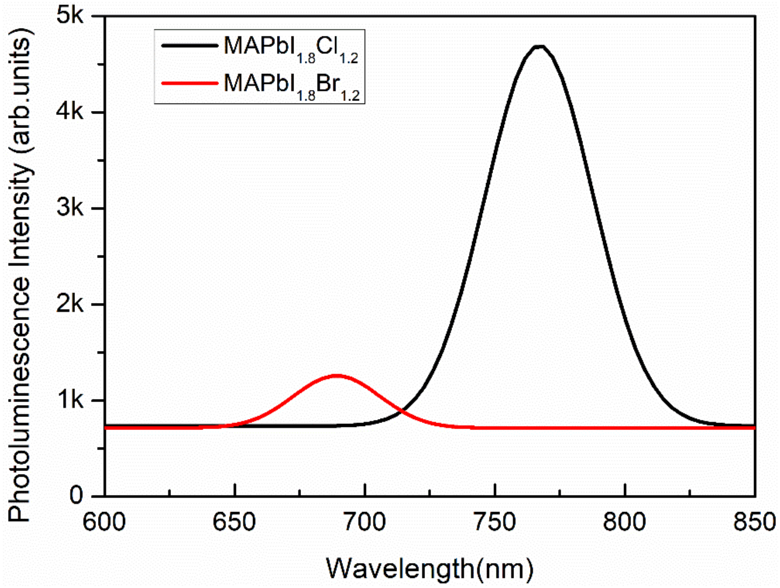

Figure 8: Photoluminescence spectra of the two different samples

Furthermore, looking at the photoluminescence spectra in figure.8, a relatively lower photoluminescence intensity is observed for the perovskite film with iodine and bromine which suggests either a low level of defects inside the perovskite layer and/or a good quenching at the n-type layer interface. This is most likely due to the absence of the PbI_2 residues (previously indicated by the XRD analysis) in this sample and the good surface quality, as observed in the morphological characterization (AFM, SEM).

The band gap energy can be calculated from the Tauc plot (figure 6a,b). The calculated optical band gap has been shifted from 1.55eV to 1.80 eV, with the bromine content, due to its lower electronegativity. According to the literature [77-79], the band gap of the ABX_3 perovskite increases as the electronegativity of the X anion decreases. Therefore, the lower electronegativity of Br induces a larger energy gap.

3.6. Solar cells performance

The effect of the second halogen, Cl / Br incorporation in the perovskite matrix on the photovoltaic properties has been investigated by current–voltage (J–V) measurements performed on the solar cells (figure.9). The average photovoltaic values obtained for 16 cells of each composition are presented and the photovoltaic parameters of the champion devices are summarized in Table 4.

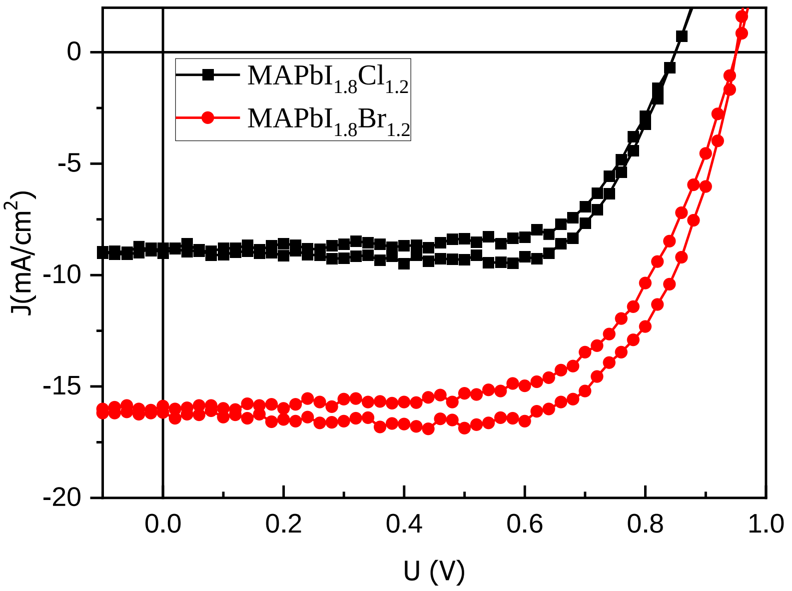

Figure 9. a) Schematic illustration of mesoscopic cells configuration, b) Forward and reserve J-V curves of champion cells with for the different composition.

Figure 9 shows the J-V characteristics of the PSCs based on $MAPbI_{1.8}Cl_{1.2}$ and $MAPbI_{1.8}Br_{1.2}$ perovskite thin films and their corresponding schematic illustration of mesoscopic cells configurations.

Table.4 photovoltaic parameters extracted from the champion and average solar cells elaborated from the different perovskite composition

Perovskite		**V_{OC} (V)**	**J_{SC} (mA/cm^2)**	**FF (%)**	**PCE (%)**
$MAPbI_{1.8}Cl_{1.2}$	**Champion device** reverse values	**0.84**	**9.02**	**71**	**5.77**
	Average between forward and reverse of champion device	*0.84*	*8.91*	*71*	*5.50*
	Average of 16 devices	0.86	8.06	72	5.01
$MAPbI_{1.8}Br_{1.2}$	**Champion device** reverse values	**0.95**	**16.17**	**69**	**10.65**
	Average between forward and reverse of champion device	*0.95*	*16.03*	*67*	*10.12*
	Average of 16 devices	*0.01*	*0.61*	*2.4*	*0.35*

The devices with $MAPbI_{1.8}Cl_{1.2}$ present a V_{OC} of 0.84 V, a short-circuit current, J_{SC} of 9.02 mA/cm^2, a fill factor, FF of 71% corresponding to a power conversion efficiency (PCE) of 5.77%. $MAPbI_{1.8}Br_{1.2}$ perovskite-based devices show a considerable higher power efficiency of, due to an improvement of all electrics parameters. Thus, an open circuit voltage (V_{OC}) of 0.95 V, a short-circuit current (J_{SC}) of 16.17 mA/cm^2, a fill factor (FF) of 74% were obtained, resulting a maximum PCE of 10.65%.

3.7. Stability evaluation

The long-term stability of the average PCE of the devices prepared from the different solutions was assessed. Figure 10 shows the evolution of the average PCE, shelf storage lifetime. The devices were stored inside the glovebox for 1200 hours and tested periodically outside, in conditions specified at the Experimental section, to investigate their long-term stability. The evolution of the average PCE during 1200 h is similar for the two compositions. Nevertheless, the degradation for the cells with $MAPbI_{1.8}Br_{1.2}$ seems to reach a plateau at 3.84 % PCE after 1200 h of storage and a loss of approximately 64% of the initial PCE. This is not the case for the $MAPbI_{1.8}Cl_{1.2}$ based device that seem to lose 92% of its initial efficiency after 1200 h and continues to degrade rapidly. This behavior of the device with bromine is owed to the compactness of the perovskite layer, with fewer defects and high structural stability.

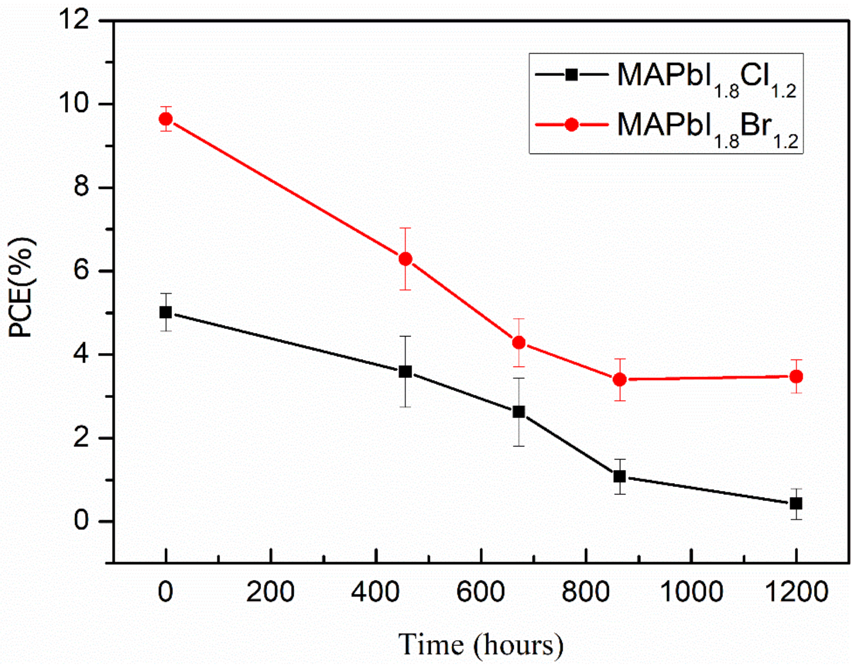

Figure 10: Stability tests of the cells with different perovskite composition

4. Conclusions

In summary, we have elaborated standard mesoscopic mixed-halide perovskite-based devices by one step spin-coating deposition method. Only by changing the type of the second added halogen, Cl or Br, but keeping the same ratio, the structural, morphological and optical properties of the perovskite film suffer dramatic changes. We have shown that the morphology of the perovskite crystallites obtained under the given processing conditions is affected considerably by the choice of the second halogen, Cl or Br, during the formation of the $MAPbI_3$ dominated perovskite films.

The use of hybrid perovskite based on mixed iodine and bromine halide in solar cells has shown a photovoltaic performance of 10.65% PCE. Compared to the cells based on mixed iodine and chlorine halide, the improved photovoltaic performance produced from $MAPbI_{1.8}Br_{1.2}$ results from the good quality of perovskite films, leading to an efficient separation of the generated charges and improved charge carrier transport.

Acknowledgments

The authors acknowledge the Romanian Ministry of Research and Innovation and UEFISCDI for financial support through the Core Program 2019-2022 (contract 21N/2019), the EEA Grants 2014–2021 under Project no. 36⁄2021, and PN-III-P2-2.1-PED-2019-1411 from Romanian Ministry of Research and Innovation. H.M. acknowledges the Romanian Ministry of Foreign Affairs and *Agence universitaire de la Francophonie* for the Eugen Ionescu research and mobility grant no. 04/ 2020 at NIMP.

References

[1] Tan, Hairen, et al. "Efficient and stable solution-processed planar perovskite solar cells via contact passivation." Science 355.6326 (2017): 722-726. (DOI: 10.1126/science. aai9081);

[2] Lv, Yinhua, et al. "Highly crystalline Nb-doped TiO_2nanospindles as superior electron transporting materials for high-performance planar structured perovskite solar cells." RSC advances 8.37 (2018): 20982-20989. (DOI: 10.1039/c8ra03559h);

[3] Lindblad, Rebecka, et al. "Electronic structure of CH3NH3PbX3 perovskites: dependence on the halide moiety." The Journal of Physical Chemistry C 119.4 (2015): 1818-1825. (DOI: 10.1021/jp509460h);

[4] Ren, Jing, et al. "Suppressing charge recombination and ultraviolet light degradation of perovskite solar cells using silicon oxide passivation." ChemElectroChem 6.12 (2019): 3167-3174. (DOI: 10.1002/celc.201900688);

[5] Tong, Jinhui, et al. "Carrier lifetimes of> 1 μs in Sn-Pb perovskites enable efficient all-perovskite tandem solar cells." Science 364.6439 (2019): 475-479. (DOI: 10.1126/science.aav7911);

[6] Gao, Liguo, et al. "Enhanced Charge Transport by Incorporating Formamidinium and Cesium Cations into Two-Dimensional Perovskite Solar Cells." Angewandte Chemie International Edition 58.34 (2019): 11737-11741. (DOI: 10.1002/anie.201905690) ;

[7] Jeong, Mingyu, et al. "Stable perovskite solar cells with efficiency exceeding 24.8% and 0.3-V voltage loss." Science 369.6511 (2020): 1615-1620. (DOI: 10.1126/science.abb7167);

[8] Kojima, Akihiro, et al. "Organometal halide perovskites as visible-light sensitizers for photovoltaic cells." Journal of the American Chemical Society 131.17 (2009): 6050-6051. (DOI: 10.1021/ja809598r);

[9] NREL, Best Research-Cell Efficiencies. https://www.nrel.gov/pv/cell-efficiency.html. (Accessed 22 August 2019);

[10] Chen, Zhaolai, et al. "Single-crystal MAPbI3 perovskite solar cells exceeding 21% power conversion efficiency." ACS Energy Letters 4.6 (2019): 1258-1259. (DOI: 10.1021/acsenergylett.9b00847)

[11] Péan, Emmanuel V., et al. "Investigating the Superoxide Formation and Stability in Mesoporous Carbon Perovskite Solar Cells with an Aminovaleric Acid Additive." Advanced Functional Materials 30.12 (2020): 1909839. (DOI: 10.1002/adfm.201909839);

[12] Wolff, Christian M., et al. "Nonradiative recombination in perovskite solar cells: the role of interfaces." Advanced Materials 31.52 (2019): 1902762. (DOI: 10.1002/adma.201902762);

[13] Maitani, Masato M., et al. "Effects of energetics with {001} facet-dominant anatase TiO2 scaffold on electron transport in CH3NH3PbI3 perovskite solar cells." Electrochimica Acta 300 (2019): 445-454. (DOI: 10.1016/j.electacta.2019.01.102);

[14] Lee, Dong Geon, et al. "Effect of TiO2 particle size and layer thickness on mesoscopic perovskite solar cells." Applied Surface Science 477 (2019) : 131-136. (DOI: 10.1016/j.apsusc.2017.11.124);

[15] Mehdi, H., et al. (2020). Effect of annealing treatment on the properties of inverted solar cells based on mixed halide perovskite. Physica E: Low-dimensional Systems and Nanostructures, 119, 114000. (DOI: 10.1016/j.physe.2020.114000);

[16] Cao, Xiaobing, et al. "High annealing temperature induced rapid grain coarsening for efficient perovskite solar cells." Journal of colloid and interface science 524 (2018): 483-489. (DOI: 10.1016/j.jcis.2018.04.019);

[17] Misra, Ravi K., et al. "Temperature-and component-dependent degradation of perovskite photovoltaic materials under concentrated sunlight." The journal of physical chemistry letters 6.3 (2015): 326-330. (DOI: 10.1021/jz502642b);

[18] Choi, Yong Chan, et al. "Controlled growth of organic–inorganic hybrid CH3 NH3 PbI3 perovskite thin films from phase-controlled cryst;alline powders." RSC Advances 6.106 (2016): 104359-104365. (DOI: 10.1039/c6ra19203c);

[19] Filonik, Oliver, et al. "Evolution of Perovskite Crystallization in Printed Mesoscopic Perovskite Solar Cells." Energy Technology 7.10 (2019): 1900343. (DOI: 10.1002/ente.201900343);

[20] Zhang, Xin, et al. "Hydrazinium salt as additive to improve film morphology and carrier lifetime for high-efficiency planar-heterojunction perovskite solar cells via one-step method." ACS applied materials & interfaces 9.42 (2017): 36810-36816. (DOI: 10.1021/acsami.7b11168);

[21] Xiao, Zhengguo, et al. "Solvent annealing of perovskite-induced crystal growth for photovoltaic-device efficiency enhancement." Advanced Materials 26.37 (2014): 6503-6509. (DOI: 10.1002/adma.201401685);

[22] Kim, Jong H., et al. "Enhanced environmental stability of planar heterojunction perovskite solar cells based on blade-coating." Advanced energy materials 5.4 (2015): 1401229. (DOI: 10.1002/aenm.201401229);

[23] Kim, Woochul, et al. "Sequential dip-spin coating method: fully infiltration of MAPbI3-xClx into mesoporous TiO2 for stable hybrid perovskite solar cells." Electrochimica Acta 245 (2017): 734-741. (DOI: 10.1016/j.electacta);

[24] Jang, Jinwoong, Geunpyo Choe, and Sanggyu Yim. "Effective Control of Chlorine Contents in MAPbI3–x Cl x Perovskite Solar Cells Using a Single-Source Vapor Deposition and Anion-Exchange Technique." ACS applied materials & interfaces 11.22 (2019): 20073-20081. (DOI: 10.1021/acsami.9b05101);

[25] Alhazmi, Noura, et al. "Perovskite Crystallization Dynamics during Spin-Casting: An In Situ Wide-Angle X-ray Scattering Study." ACS applied energy materials 3.7 (2020): 6155-6164. (DOI: 10.1021/acsaem.9b02470);

[26] Alhazmi, Noura, et al. "Perovskite Crystallization Dynamics during Spin-Casting: An In Situ Wide-Angle X-ray Scattering Study." ACS applied energy materials 3.7 (2020): 6155-6164. (DOI: 10.1021/acsaem.9b02470);

[27] Pammi, Sri Venkata Narayana, et al. "Bromine Doping of MAPbI3 Films Deposited via Chemical Vapor Deposition Enables Efficient and Photo-Stable Self-Powered Photodetectors." Advanced Optical Materials 8.19 (2020): 2000845. (DOI: 10.1002/adom.202000845);

[28] Cerdán-Pasarán, Andrea, et al. "Improved performance of inverted planar MAPbI3 based perovskite s. olar cells using bromide post-synthesis treatment." Solar Energy 177 (2019): 538-544. (DOI: 10.1016/j.solener.2018.11.025);

[29] Mehdi, Hanadi, Asya Mhamdi, and Abdelaziz Bouazizi. "Effect of perovskite precursor ratios and solvents volume on the efficiency of MAPbI3-xClx mixed halide perovskite solar cells." Materials Science in Semiconductor Processing 109 (2020): 104915. (DOI: 10.1016/j.mssp.2020.104915);

[30] Tavakoli, M. M., Yadav, P., Prochowicz, D., Sponseller, M., Osherov, A., Bulović, V., & Kong, J. (2019). Controllable perovskite crystallization via antisolvent technique using chloride additives for highly efficient planar perovskite solar cells. Advanced Energy Materials, 9(17), 1803587. (DOI: 10.1002/aenm.201803587);

[31] Umemoto, Yuri, Atsushi Suzuki, and Takeo Oku. "Effects of halogen doping on the photovoltaic properties of HC (NH2) 2PbI$_3$ perovskite solar cells." AIP Conference Proceedings. Vol. 1807. No. 1. AIP Publishing LLC, 2017. (DOI: 10.1063/1.4974793);

[32] Chen, Jing, et al. "Halogen versus pseudo-halogen induced perovskite for planar heterojunction solar cells: some new physical insights." The Journal of Physical Chemistry C 121.51 (2017): 28443-28453. (DOI: 10.1021/acs.jpcc.7b10018);

[33] Cho, Junsang, and Prashant V. Kamat. "How Chloride Suppresses Photoinduced Phase Segregation in Mixed Halide Perovskites." Chemistry of Materials 32.14 (2020): 6206-6212. (DOI: 10.1021/acs.chemmater.0c02100);

[34] Lee, Byungho, et al. "Microstructural evolution of hybrid perovskites promoted by chlorine and its impact on the performance of solar cell." Scientific reports 9.1 (2019): 1-8. (DOI: 10.1038/s41598-019-41328-5);

[35] Soltanpoor, Wiria, et al. "Hybrid vapor-solution sequentially deposited mixed-halide perovskite solar cells." ACS Applied Energy Materials 3.9 (2020): 8257-8265. (DOI: 10.1021/acsaem.0c00686);

[36] Spalla, Manon, et al. "Alternative electron transport layer based on Al-doped ZnO and SnO2 for perovskite solar cells: impact on microstructure and stability." ACS Applied Energy Materials 2.10 (2019): 7183-7195. (DOI: 10.1021/acsaem.9b01160);

[37] Huang, Yulan, et al. "Towards Simplifying the Device Structure of High-Performance Perovskite Solar Cells." Advanced Functional Materials (2020): 2000863. (DOI: 10.1002/adfm.202000863);

[38] Kothandaraman, Radha K., et al. "Near-Infrared-Transparent Perovskite Solar Cells and Perovskite-Based Tandem Photovoltaics." Small Methods 4.10 (2020): 2000395. (DOI: 10.1002/smtd.202000395);

[39] Lu, Chunyuan, et al. "Well-grown low-defect MAPbI3–xClx films for perovskite solar cells with over 20% efficiency fabricated under controlled ambient humidity conditions." Electrochimica Acta 326 (2019): 134950. (DOI: 10.1016/j.electacta.2019.134950);

[40] Jang, Jinwoong, Geunpyo Choe, and Sanggyu Yim. "Effective Control of Chlorine Contents in MAPbI3–x Cl x Perovskite Solar Cells Using a Single-Source Vapor Deposition and Anion-Exchange Technique." ACS applied materials & interfaces 11.22 (2019): 20073-20081. (DOI: 10.1021/acsami.9b05101);

[41] Xie, Yue-Min, et al. "Revealing the crystallization process and realizing uniform 1.8 eV MA-based wide-bandgap mixed-halide perovskites via solution engineering." Nano Research 12.5 (2019): 1033-1039. (DOI: 10.1007/s12274-019-2336-5);

[42] Alidaei, Maryam. "Increasing of solar cell stability using Br-doped CH3NH3PbI3 perovskite absorber layers." Iranian Journal of Crystallography and Mineralogy 27.1 (2019): 231-244. (DOI: 10.29252/ijcm.27.1.231);

[43] Khan, Abbas Ahmad, et al. "Solution-processed photodetector based on Br incorporated perovskite materials." AOPC 2019: Nanophotonics. Vol. 11336. International Society for Optics and Photonics, 2019. (DOI: 10.1117/12.2547655);

[44] Li, Chongwen, et al. "Reducing saturation-current density to realize high-efficiency low-bandgap mixed tin–lead halide perovskite solar cells." Advanced Energy Materials 9.3 (2019): 1803135. (DOI: 10.1002/aenm.201803135);

[45] Goetz, Katelyn P., et al. "Shining Light on the Photoluminescence Properties of Metal Halide Perovskites." Advanced Functional Materials (2020): 1910004. (DOI: 10.1002/adfm.201910004);

[46] Tombe, Sekai, et al. "Optical and electronic properties of mixed halide (X= I, Cl, Br) methylammonium lead perovskite solar cells." Journal of Materials Chemistry C 5.7 (2017): 1714-1723. (DOI: 10.1039/C6TC04830G);

[47] Xi, Jun, et al. "Deciphering perovskite crystal growth in interdiffusion protocol for planar heterojunction photovoltaic devices." Organic Electronics 53 (2018): 88-95. (DOI: 10.1016/j.orgel.2017.11.011);

[48] Kogo, Atsushi, and Masayuki Chikamatsu. "Electron band tuning of organolead halide perovskite materials by methylammonium and formamidinium halide post-treatment for high-efficiency solar cells." Chemical Communications 56.8 (2020): 1235-1238. (DOI: 10.1039/C9CC09002A);

[49] Fan, Zhengfang, et al. "Mixed-Cation MAxCs1− xPbBr3 Perovskite Single Crystals with Composition Management for High-Sensitivity X-Ray Detection." physica status solidi (RRL)–Rapid Research Letters 14.10 (2020): 2000226. (DOI: 10.1002/pssr.202000226);

[50] Li, Chongwen, et al. "Low-bandgap mixed tin–lead iodide perovskites with reduced methylammonium for simultaneous enhancement of solar cell efficiency and stability." Nature Energy 5.10 (2020): 768-776 (DOI: 10.1038/s41560-020-00692-7);

[51] Li, Yanbo, et al. "Fabrication of planar heterojunction perovskite solar cells by controlled low-pressure vapor annealing." The journal of physical chemistry letters 6.3 (2015): 493-499. (DOI: 10.1021/jz502720a);

[52] Mosconi, Edoardo, Enrico Ronca, and Filippo De Angelis. "First-principles investigation of the TiO2/organohalide perovskites interface: The role of interfacial chlorine." The journal of physical chemistry letters 5.15 (2014): 2619-2625. (DOI:10.1021/jz501127k);

[53] Mosconi, Edoardo, et al. "First-principles modeling of mixed halide organometal perovskites for photovoltaic applications." The Journal of Physical Chemistry C 117.27 (2013): 13902-13913. (doi.org/10.1021/jp4048659);

[54] Sedighi, Rahime, et al. "Mixed-Halide CH3NH3PbI3− xXx (X= Cl, Br, I) Perovskites: Vapor-Assisted Solution Deposition and Application as Solar Cell Absorbers." ChemPhysChem 17.15 (2016): 2382-2388. (DOI: 10.1002/cphc.201600230);

[55] Cao, Kun, et al. "MAPbI 3− x Br x mixed halide perovskites for fully printable mesoscopic solar cells with enhanced efficiency and less hysteresis." Nanoscale 8.16 (2016): 8839-8846. (DOI: 10.1002/cphc.201600230);

[56] Tombe, Sekai, et al. "The influence of perovskite precursor composition on the morphology and photovoltaic performance of mixed halide MAPbI3-xClx solar cells." Solar Energy 163 (2018): 215-223. (DOI: 10.1016/j.solener.2018.01.083);

[57] Liang, Po-Wei, et al. "High-Performance Planar-Heterojunction Solar Cells Based on Ternary Halide Large-Band-Gap Perovskites." Advanced Energy Materials 5.1 (2015): 1400960. (DOI: 10.1002/aenm.201400960);

[58] Spalla, Manon, et al. "Influence of Chloride/Iodide Ratio in MAPbI3-xClx Perovskite Solar Devices: Case of Low Temperature Processable AZO Sub-Layer." Energies 13.8 (2020): 1927. (DOI:10.3390/en13081927);

[59] Nemnes, George Alexandru, et al. "How measurement protocols influence the dynamic JV characteristics of perovskite solar cells: Theory and experiment." Solar Energy 173 (2018): 976-983. (DOI: 10.1016/j.solener.2018.08.033) ;

[60] Tomulescu, Andrei Gabriel, et al. "Reticulated Mesoporous TiO2 Scaffold, Fabricated by Spray Coating, for Large-Area Perovskite Solar Cells." Energy Technology 8.1 (2020): 1900922. (DOI:10.1002/ente.201900922);

[61] Maculan, Giacomo, et al. "CH3NH3PbCl3 single crystals: inverse temperature crystallization and visible-blind UV-photodetector." The journal of physical chemistry letters 6.19 (2015): 3781-3786. (DOI: 10.1021/acs.jpclett.5b01666);

[62] López, Carlos A., et al. "Elucidating the methylammonium (MA) conformation in MAPbBr3 perovskite with application in solar cells." Inorganic chemistry 56.22 (2017): 14214-14219. (DOI: 10.1021/acs.inorgchem.7b02344);

[63] Chen, Qi, et al. "The optoelectronic role of chlorine in CH3NH3PbI3(Cl)-based perovskite solar cells." Nature communications 6.1 (2015): 1-9. (DOI:10.1038/ncomms8269);

[64] Speakman, Scott A. "Estimating crystallite size using XRD."MIT Center for Materials Science and Engineering (2014): 03-08 (http://prism.mit.edu/XRAY/oldsite/CrystalSizeAnalysis.pdf);

[65] Vashista, M., and S. Paul. "Correlation between full width at half maximum (FWHM) of XRD peak with residual stress on ground surfaces." Philosophical Magazine 92.33 (2012): 4194-4204. (DOI : 10.1080/14786435.2012.704429);

[66] Travis, W., et al. "On the application of the tolerance factor to inorganic and hybrid halide perovskites: a revised system." Chemical Science 7.7 (2016) :4548-4556. (DOI: 10.1039/c5sc04845a);

[67] Nagabhushana, G. P., et al. "Direct calorimetric verification of thermodynamic instability of lead halide hybrid perovskites." Proceedings of the National Academy of Sciences 113.28 (2016): 7717-7721. (DOI: 10.1073/pnas.1607850113);

[68] Wang, Chunhua, et al. "Air-induced high-quality CH3NH3PbI3 thin film for efficient planar heterojunction perovskite solar cells." The Journal of Physical Chemistry C 121.12 (2017): 6575-6580. (DOI: 10.1021/acs.jpcc.7b00981);

[69] Zhou, Ning, et al. "CsI Pre-Intercalation in the Inorganic Framework for Efficient and Stable FA1− x CsxPbI3 (Cl) Perovskite Solar Cells." Small 13.23 (2017): 1700484. (DOI:10.1002/smll.201700484);

[70] Wang, Dong, et al. "Reproducible One-Step Fabrication of Compact MAPbI3–x Cl x Thin Films Derived from Mixed-Lead-Halide Precursors." Chemistry of Materials 26.24 (2014): 7145-7150. (DOI:/10.1021/cm5037869);

[71] Eperon, G. E., Burlakov, V. M., Docampo, P., Goriely, A., & Snaith, H. J. (2014). Morphological control for high performance, solution-processed planar heterojunction perovskite solar cells. Advanced Functional Materials, 24(1), 151-157. (DOI: 10.1002/adfm.201302090);

[72] Gao, Peng, Michael Grätzel, and Mohammad K. Nazeeruddin. "Organohalide lead perovskites for photovoltaic applications." Energy & Environmental Science 7.8 (2014): 2448-2463. (DOI : 10.1039/c4ee00942h);

[73] Mohebpour, Mohammad Ali, et al. "High performance of mixed halide perovskite solar cells: Role of halogen atom and plasmonic nanoparticles on the ideal current density of cell." Physica E: Low-dimensional Systems and Nanostructures 97 (2018): 282-289. (DOI: 10.1016/j.physe.2017.11.022);

[74] Lv, Minghang, et al. "A promising alternative solvent of perovskite to induce rapid crystallization for high-efficiency photovoltaic devices." RSC Advances 5.26 (2015): 20521-20529. (DOI: 10.1039/C4RA16253F);

[75] D'Innocenzo, Valerio, et al. "Tuning the light emission properties by band gap engineering in hybrid lead halide perovskite." Journal of the American Chemical Society 136.51 (2014): 17730-17733. (DOI: 10.1021/ja511198f);

[76] Wu, Kewei, et al. "Temperature-dependent excitonic photoluminescence of hybrid organometal halide perovskite films." Physical Chemistry Chemical Physics 16.41 (2014): 22476-22481. (DOI: 10.1039/c4cp03573a);

[77] Gamliel, Shany, et al. "Micrometer sized perovskite crystals in planar hole conductor free solar cells." The Journal of Physical Chemistry C 119.34 (2015): 19722-19728. (DOI: 10.1021/acs.jpcc.5b07554);

[78] Gao, Peng, Michael Grätzel, and Mohammad K. Nazeeruddin. "Organohalide lead perovskites for photovoltaic applications." Energy & Environmental Science 7.8 (2014): 2448-2463. (DOI: 10.1039/C4EE00942H);

[79] Jung, Hyun Suk, and Nam-Gyu Park. "Perovskite solar cells: from materials to devices." small 11.1 (2015): 10-25. (DOI: 10.1002/smll.201402767);